Bubble Formation in a Coflow Configuration in Normal and Reduced Gravity

Avijit Bhunia, Salvatore C. Pais, Yasuhiro Kamotani, and Iee-Hwan Kim
Dept. of Mechanical and Aerospace Engineering, Case Western Reserve University, Cleveland, OH 44106

A study of bubble generation for constant gas-flux condition by single-nozzle injection in a coflowing liquid is reported. Focusing on single-bubble generation in the dynamic and bubbly flow regime, the onset condition for bubble coalescence is investigated. The role of various forces involved in the bubble formation process is studied, and an overall force balance describing bubble dynamics is developed. Gas-momentum flux and buoyancy in normal gravity enhance, while the surface-tension force at the nozzle rim inhibits bubble detachment. On the other hand, liquid drag and inertia can act both as attaching or detaching forces, depending on the relative velocity of the bubble with respect to the surrounding liquid. Predictions of the theoretical model compare well with the present reduced-gravity experiment and available normal-gravity experiments. Effects of the fluid properties, injection geometry, and flow conditions on bubble size are investigated.

Introduction

Situations where a gas and a liquid flow together in a pipe occur in various terrestrial applications, such as gas dissolution in liquid in the chemical and pharmaceutical industries (Clift et al., 1978), oil and gas pipelines (Hill, 1997), nuclear power plants, and two-phase flow heat exchangers, to name a few examples. Although many experimental and theoretical studies have been carried out to examine gas–liquid flows on earth, there is still a lack of understanding as to why many of the observed phenomena occur, making such flows extremely difficult to predict accurately. In parallel, two-phase flow systems are also widely used for various current and potential space applications, such as power generation, propulsion, thermal management, cryogenic storage, and life-support systems aboard spacecraft. Currently, the thermal management system is handled by a single-phase pumped liquid loop. A better alternative to the present practice is to employ a two-phase gas–liquid thermal control system (Ostrach, 1988; Banerjee, 1989). The primary advantage of a two-phase system lies in the large amounts of energy that are transferred by boiling and condensation processes. Thus the system operates with a smaller volume of liquid and at a lower flow rate, which gives rise to system weight reduction. Based on this idea, in recent years the NASA microgravity science program has given considerable attention to research on the capillary pump loop concept as an alternative to the conventional heat pipe (Herold and Kolos, 1997). The need to understand bubble generation under microgravity conditions arises from the fact that for all these applications, the size and distribution of bubbles are extremely crucial in the process of heat and mass transfer, pressure drop, and flow pattern transitions.

Under microgravity conditions, with reduced buoyancy, larger and more spherical bubbles are generated, sometimes leading to the formation of bubbles that are longer than the pipe diameter (Taylor bubbles). Therefore, to control bubble size and frequency, an additional force is needed for detachment, namely the drag induced by the liquid flowing through the conduit as discussed by Kim et al. (1994). Two configurations generally used for bubble dispersion in a flowing liquid are the coflow and cross-flow geometries. In coflow, the dispersed phase is introduced through a nozzle in the same direction as the liquid flow, whereas in the cross-flow configuration, gas is injected perpendicular to the direction of liquid flow.

Bubble formation due to gas injection can be divided into three conditions: constant flow, constant pressure, and intermediate conditions (Kumar and Kuloor, 1970). At constant flow conditions, studied in this article, the volumetric gas flow rate remains fixed throughout the bubble formation process. Depending on the gas flux rate, there are three known regimes of bubble generation: the static, dynamic, and turbulent

Correspondence concerning this article should be addressed to Y. Kamotani.

regimes. The static regime occurs at very low flow rates, typically smaller than 1 cm^3/s (Van Krevelen and Hoftijzer, 1950), whereas a high gas flow rate corresponds to the turbulent regime. Of practical importance is the dynamic regime, which extends from 1 cm^3/s to about 10^4 cm^3/s for an air–water system (Wraith, 1971). The dynamic regime can further be divided into two subregimes, such as single-bubble, including pairing, and double-bubble (McCann and Prince, 1971). In the single-bubble subregime, which occurs at low gas flow rates, uniformly spaced bubbles of approximately equal size are produced. At higher gas flow rates, that is, in the double-bubble subregime, two bubbles coalesce at the nozzle exit. With an increasing gas flow rate, bubble coalescence becomes more frequent, eventually forming a gas jet, thereby leading to a transition from the dynamic to the turbulent regime. The present work concentrates on single-bubble formation and presents an experimentally observed mechanism for the onset condition of coalescence. Under reduced and microgravity conditions, a single bubble can grow larger than the pipe diameter before detachment, thereby forming a Taylor bubble. A Taylor bubble can also be formed by coalescence. The inception of a Taylor bubble characterizes the transition from bubbly to slug flow, which has been extensively studied by Dukler et al. (1988), Colin et al. (1991), and very recently by Jayawardena et al. (1997).

Bubble generation by a nozzle injection in a quiescent liquid has been extensively studied in the past. A compendium of pertinent literature is presented by Tsuge (1986) and Räbiger and Vogelpohl (1986). More recently Pamperin and Rath (1995) investigated the influence of buoyancy on bubble detachment criteria. Along the same line Buyevich and Webbon (1996) concluded that the gas-momentum flux and the buoyancy force are critical detaching forces in a quiescent liquid. Furthermore, they observed that under reduced gravity conditions, gas flux is the only detaching mechanism, which necessitates the presence of another detaching force to control bubble volume and frequency. Bubble formation in the cross-flow configuration has been studied by Al-Hayes and Winterton (1981), Kawase and Ulbrecht (1981), and Kim et al. (1994), among other investigators. At the same time, vapor bubble departure in convective boiling that displays the cross-flow geometry also has been studied by Klausner et al. (1993) and others.

On the other hand, the coflow configuration has not been as extensively studied as the cross-flow geometry. Chuang and Goldschmidt (1970) proposed a model for bubble formation in a coflowing liquid under normal gravity conditions. Sada et al. (1978) experimentally observed the effect of liquid velocity on bubble detachment in a coflow configuration and reported a decrease in bubble diameter with flowing liquid. However, the ensuing transport phenomena are still not well understood. Under microgravity conditions, bubble generation and the resulting two-phase flow by multiple-nozzle injection along the periphery of the flow conduit has been studied by several investigators and summarized by Colin et al. (1996). With multiple injection, it is difficult to control void fraction of the dispersed phase due to coalescence of adjacent bubbles. A better alternative is controlled bubble generation by single nozzle injection (Pais, 1998).

In the present work, bubble generation by gas injection through a single nozzle in a coflowing liquid is investigated. Experiments are performed aboard the Reduced Gravity Research Aircraft at NASA Lewis Research Center. The theoretical work considers at two-stage model for bubble generation, the expansion stage, and the detachment stage (Ramakrishnan et al., 1969). The present numerical work is valid in the bubbly flow regime and predicts a bubble diameter up to the transition point to slug flow. Based on the overall balance of forces acting on the bubble at the two stages, the final bubble diameter is computed. The computational results show good agreement with the current reduced-gravity and available normal-gravity experimental data. Effects of the fluid properties, injection geometry, and flow conditions on bubble size are investigated.

Theoretical Model

In the coflow configuration, a nozzle of diameter D_N is located at the center of a circular pipe of diameter D_P. A liquid of density ρ_c, dynamic viscosity μ_c, and surface tension σ flows through the pipe at a constant superficial liquid velocity U_{LS} and volumetric flow rate $Q_c[=(\pi/4)D_P^2U_{LS}]$. In the same direction of the liquid flow, a gas of density ρ_d and dynamic viscosity μ_d is injected at a constant volumetric flow rate Q_d through the nozzle. The bubble formation in a coflow system is shown in Figure 1. In order to compare the predictions of the present theoretical model with the experimental results of Sada et al. (1978) under terrestrial conditions, the gravity vector is considered in the same direction as their experiment. Under reduced gravity conditions the gravity vector is reduced to only 1% of that in terrestrial environment and therefore the directional effect of the gravity vector on the bubble diameter is minimal.

An exact theoretical approach to describe the bubble and surrounding liquid motion before and after bubble detachment is highly complicated. Based on certain simplifying assumptions, the theoretical model developed in this section considers an engineering approach, yet focuses on the impor-

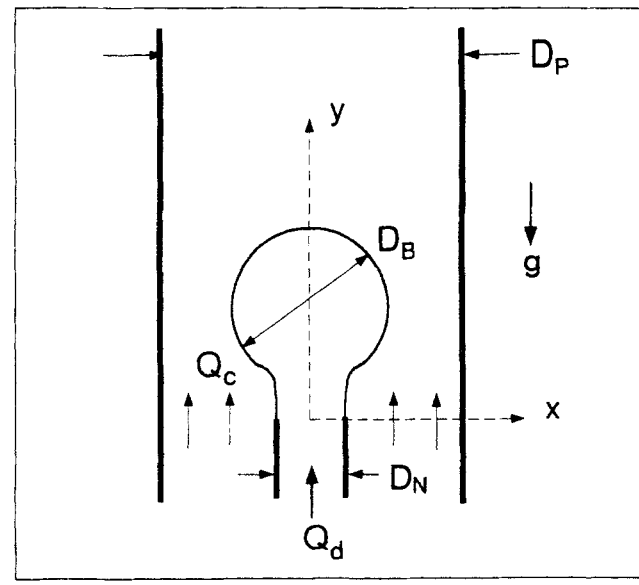

Figure 1. Bubble formation by single-nozzle injection in a coflow geometry.

tant fluid mechanics aspects of the problem. The key point of the model lies in identifying various forces involved in the process of detachment and on describing bubble motion due to these forces. The bubble shape is assumed to be spherical throughout the formation process. Thus, for the constant flow condition, the rate of change of bubble volume is given as

$$\frac{dV_B}{dt} = \frac{d}{dt}\left[\frac{\pi}{6} D_B^3(t)\right] = Q_d = \text{Constant}, \tag{1}$$

where V_B is the volume and $D_B(t)$ is the diameter of the forming bubble.

The present model is based on a balance of forces acting on the bubble. Forces acting on the bubble can be categorized into two groups. One set of forces favoring bubble detachment are termed detaching or positive forces, while the others opposing detachment are called attaching or negative forces. The important forces and their characteristics are identified as follows:

$$\text{Buoyancy force} = F_B = V_B(\rho_c - \rho_d)g, \tag{2}$$

where g is the acceleration due to gravity in a terrestrial environment. Under reduced gravity and microgravity conditions, acceleration due to gravity is reduced to $0.01g$ and $10^{-4}g$, respectively. The buoyancy force acts vertically upwards and is detaching in nature.

$$\text{Surface-tension force} = F_\sigma = \pi D_N \sigma. \tag{3}$$

The surface-tension force, acting along the nozzle rim, pulls the bubble toward the injector, thereby acting as an attaching force.

$$\text{Momemtum flux} = F_M = \rho_d \frac{Q_d^2}{\frac{\pi}{4} D_N^2}. \tag{4}$$

This force acts in the direction of injection, and hence is a detaching force.

$$\text{Inertia force} = F_I = \frac{d}{dt}\left(\rho_d V_B \frac{ds}{dt}\right) + \frac{d}{dt}\left[\rho_c C_{MC} V_B \left(\frac{ds}{dt} - U_{LS}\right)\right], \tag{5}$$

where ds/dt is the velocity of bubble center away from the origin located at the nozzle tip and C_{MC} is the added mass coefficient. Equation 5 shows that inertia consists of two parts. The first term is the inertia due to bubble motion, called bubble inertia. The second term is for inertia of the liquid that is pushed by the accelerating surface of the expanding bubble, hereafter called liquid inertia. The added mass coefficient for the coflow configuration, developed by Kim (1992), is given as

$$C_{MC} = \frac{1}{2} + 3\left(1 + \frac{1}{2\sqrt{2}}\right)\left(\frac{1}{\pi}\right)^{3/2} \bar{D}_B^3(t), \tag{6}$$

where $\bar{D}_B$ is the dimensionless bubble diameter, nondimensionalized as the ratio of bubble to pipe diameters. For a sphere moving in an infinite liquid, the value of C_{MC} is 1/2. The effect of the confining walls is taken into consideration in the second term of Eq. 6. The bubble inertia is attaching, while the liquid inertia force could be attaching or detaching depending on the relative magnitude of the velocity of bubble center ds/dt and superficial liquid velocity U_{LS}.

$$\text{Drag force} = F_D = S_D C_{DW} \frac{1}{2} \rho_c U_{\text{eff}}^2 A_{\text{eff}} \tag{7}$$

where C_{DW} is the drag coefficient, U_{eff} is the relative velocity of a forming bubble with respect to the coflowing liquid, A_{eff} is the effective cross-sectional area of the bubble over which the drag force acts, and $S_D = +1$ or -1 for $U_{\text{eff}} < 0$ and $U_{\text{eff}} > 0$, respectively. The effect of the confining pipe wall on drag force is taken into consideration in formulating the drag coefficient C_{DW}. Following the empirical relation of Clift et al. (1978), the expression for C_{DW}, developed by Kim (1992) and Kim et al. (1994), is

$$C_{DW} = C_D \frac{1}{(1 - \bar{D}_B^2)^3}, \tag{8}$$

where C_D is the drag coefficient of a bubble moving through a liquid of infinite expanse. Several correlations for the drag coefficient of spherical bubbles and drops moving through an infinite liquid are available in the literature (Clift et al., 1978). Similarly, the literature on drag coefficient for a solid sphere moving through a quiescent infinite liquid is also reported by various authors and summarized by Bird et al. (1960). Results computed in the present model are compared with current experimental data using drag coefficients of both bubble and solid sphere. It is observed that bubble diameters predicted using the drag coefficient of a solid sphere are in better agreement with experimental results, both under normal- and reduced-gravity conditions. In general, due to the internal circulation of gas inside the bubble, the drag coefficient of a bubble moving within a liquid is less than that for a solid sphere. However, in the present problem, it is believed that the circulation within the bubble is disturbed by the injected gas-momentum flux. A similar observation was also reported by Ramakrishnan et al. (1969) and Kim et al. (1994). The surface of the bubble may also be partially immobilized due to presence of surface contamination. These two effects combine to cause the bubble to behave like a solid sphere. The drag coefficients used in this model are

$$\begin{aligned} C_D &= \frac{24}{Re_B} && \text{for} \quad Re_B < 2 \\ &= \frac{18.5}{Re_B^{0.6}} && \text{for} \quad 2 \le Re_B \le 500 \\ &= 0.44 && \text{for} \quad 500 \le Re_B < 2{,}000. \end{aligned} \tag{9}$$

Here Re_B is the Reynolds number based on bubble diameter, written as $Re_B = \rho_c U_{\text{eff}} D_B(t)/\mu_c$. Relative velocity of the

bubble with respect to the surrounding liquid U_{eff} is written as

$$U_{\text{eff}} = \frac{ds}{dt} - U_{LS}. \tag{10}$$

Relative velocity U_{eff} can be positive or negative depending on the magnitude of ds/dt and U_{LS}. When the bubble velocity is greater than the liquid velocity, the bubble front has to push the liquid and thus in turn experiences a drag force that prevents detachment. On the other hand, if the liquid velocity is higher, the surrounding liquid pulls the bubble front away from the nozzle tip, and thus the drag force acts as a detaching force. Depending on whether the drag force is attaching or detaching, the frontal area of the bubble that experiences the drag force changes. The effective area is

$$\begin{aligned} A_{\text{eff}} &= \frac{\pi}{4} D_B^2(t) && \text{for} \quad U_{\text{eff}} > 0 \\ &= \frac{\pi}{4}[D_B^2(t) - D_N^2] && \text{for} \quad U_{\text{eff}} < 0. \end{aligned} \tag{11}$$

After a bubble detaches and moves away from the nozzle, it initiates a drift flow in its wake, as discussed by Hahne and Grigull (1977). This drift flow, in turn, induces a suction effect and acts as a detaching force for the forming bubble. Zeng et al. (1993) gave an estimate of this lift force and showed that this force is very small compared to the other forces previously discussed. Therefore, in this model, the lift force created by the wake of the preceding bubble is neglected.

In the present model, bubble formation is assumed to take place in two stages—the expansion stage and the detachment stage. During the expansion stage, the bubble grows radially due to incoming gas flux, but the bubble base remains attached to the nozzle. This stage ends when the sum of attaching and detaching forces balance each other. During the expansion stage $V_B = \pi/6\, D_B^3(t)$ and $ds/dt = 1/2\, dD_B(t)/dt$. Thus, the force balance equation at the end of expansion stage is

$$\begin{aligned} &\frac{d}{dt}\left[\rho_d \frac{\pi}{6} D_B^3(t) \frac{1}{2} \frac{dD_B(t)}{dt} \right. \\ &\qquad \left. + \rho_c C_{MC} \frac{\pi}{6} D_B^3(t) \left(\frac{1}{2}\frac{dD_B(t)}{dt} - U_{LS}\right)\right] \\ &+ \pi D_N \sigma = \rho_d \frac{Q_d^2}{\frac{\pi}{4} D_N^2} + \frac{\pi}{6} D_B^3(t)(\rho_c - \rho_d) g \\ &\qquad + S_D C_{DW} \frac{1}{2} \rho_c \left(\frac{1}{2}\frac{dD_B(t)}{dt} - U_{LS}\right)^2 A_{\text{eff}}. \end{aligned} \tag{12}$$

The end of the expansion stage brings in the detachment phase. During the detachment phase, additional gas is fed into the bubble, which continues to grow in size. The bubble moves away from the nozzle, but still remains attached to it through a neck, which also grows with time. During the detachment phase, part of the gas injected through the nozzle goes into increasing the bubble volume, while the rest adds to the neck size. Over the period of detachment, however, the increase in neck volume is negligibly small compared to the bubble volume. Therefore, it is assumed that the entire gas flow adds toward increasing bubble size. Thus, bubble volume during the detachment stage is $V_B = (\pi/6\, D_{Be}^3 + Q_d t)$, where D_{Be} is the bubble diameter at the end of expansion stage. The bubble center, located at a distance Y from the nozzle tip, moves at a velocity $ds/dt = dY/dt$, which is faster than $1/2 dD_B(t)/dt$. Bubble motion at this stage is expressed by Newton's Second Law:

$$\begin{aligned} &\frac{d}{dt}\left[\rho_d\left(\frac{\pi}{6} D_{Be}^3 + Q_d t\right)\frac{dY}{dt} \right. \\ &\qquad \left. + \rho_c C_{MC}\left(\frac{\pi}{6} D_{Be}^3 + Q_d t\right)\left(\frac{dY}{dt} - U_{LS}\right)\right] \\ &+ \pi D_N \sigma = \rho_d \frac{Q_d^2}{\frac{\pi}{4} D_N^2} + \left(\frac{\pi}{6} D_{Be}^3 + Q_d t\right)(\rho_c - \rho_d) g \\ &\qquad + S_D C_{DW} \frac{1}{2} \rho_c \left(\frac{dY}{dt} - U_{LS}\right)^2 A_{\text{eff}}. \end{aligned} \tag{13}$$

At the end of the second stage, the neck pinches off and the bubble detaches. Following the detachment criterion discussed by Kim (1992) and Kim et al. (1994), it is assumed that the bubble neck collapses when the neck length becomes equal to the nozzle diameter, that is,

$$L_N = Y - \frac{1}{2} D_B \geq D_N. \tag{14}$$

The force-balance equations for the expansion stage, Eq. 12, detachment stage, Eq. 13, and the detachment criterion, Eq. 14, are cast into dimensionless form by nondimesionalizing with respect to reference length $L_R = D_P$, reference time $t_R = D_P/U_{LS}$, and reference force $F_R = \rho_c U_{LS}^2 D_P^2$. The nondimensional forms of Eqs. 12, 13, and 14 are, respectively,

$$\begin{aligned} &\frac{\pi}{96}\frac{\bar{U}_{GS}^2}{\bar{D}_B^2}(8C_{MC} + 2\bar{\rho} - 3) - \frac{\pi}{8}\bar{U}_{GS}(4C_{MC} - 1) + \frac{\pi \bar{D}_N}{We_p} \\ &= \frac{\pi}{4}\bar{\rho}\left(\frac{\bar{U}_{GS}}{\bar{D}_N}\right)^2 + \frac{\pi}{6}\frac{\bar{D}_B^3}{Fr_p} + S_D C_{DW}\frac{1}{2}\left[\frac{1}{4}\frac{\bar{U}_{GS}}{\bar{D}_B^2} - 1\right]^2 \bar{A}_{\text{eff}} \end{aligned} \tag{15}$$

$$\begin{aligned} &\frac{\pi}{6}(C_{MC} + \bar{\rho})\left(\bar{D}_{Be}^3 + \frac{3}{2}\bar{U}_{GS}\bar{t}\right)\frac{d^2\bar{Y}}{d\bar{t}^2} \\ &\quad + \frac{\pi}{4}\bar{U}_{GS}\left(2C_{MC} + \bar{\rho} - \frac{1}{2}\right)\frac{d\bar{Y}}{d\bar{t}} - \frac{\pi}{4}\bar{U}_{GS}\left(2C_{MC} - \frac{1}{2}\right) \\ &\quad + \frac{\pi \bar{D}_N}{We_p} = \frac{\pi}{6}\frac{\left(\bar{D}_{Be}^3 + \frac{3}{2}\bar{U}_{GS}\bar{t}\right)}{Fr_p} + \frac{\pi}{4}\bar{\rho}\left(\frac{\bar{U}_{GS}}{\bar{D}_N}\right)^2 \\ &\qquad + S_D C_{DW}\frac{1}{2}\left(\frac{d\bar{Y}}{d\bar{t}} - 1\right)^2 \bar{A}_{\text{eff}} \end{aligned} \tag{16}$$

and

$$\bar{L}_N = \bar{Y} - \frac{1}{2}\bar{D}_B \geq \bar{D}_N. \tag{17}$$

Various nondimensional parameters are superficial gas velocity $\bar{U}_{GS} = U_{GS}/U_{LS} = Q_d/Q_c = (4Q_d/\pi D_P^2)/(4Q_c/\pi D_P^2)$; nondimensional bubble diameter $\bar{D}_B = D_B/D_P$; density ratio $\bar{\rho} = \rho_d/\rho_c$; nondimensional nozzle diameter $\bar{D}_N = D_N/D_P$; Weber number $We_P = \rho_c U_{LS}^2 D_P/\sigma$; Froude number $Frp = \rho_c U_{LS}^2/(\rho_c - \rho_d)gD_P$; nondimensional effective area $\bar{A}_{\text{eff}} = \pi/4\ (\bar{D}_B^2 - \bar{D}_N^2)$ for $\bar{U}_{\text{eff}} < 0$ and $\bar{A}_{\text{eff}} = \pi/4\,\bar{D}_B^2$ for $\bar{U}_{\text{eff}} > 0$; nondimensional bubble diameter at the end of expansion stage $\bar{D}_{Be} = D_{Be}/D_P$; nondimensional time $\bar{t} = tU_{LS}/D_P$; dimensionless bubble center location $\bar{Y} = Y/D_P$; and Reynolds number $Re_p = \rho_c U_{LS} D_P/\mu_c$. The Reynolds number Re_P does not directly appear in any of the preceding equations. However, the drag coefficient C_{DW} is a function of the Reynolds number based on bubble diameter Re_B, as shown in Eq. 9. The two Reynolds numbers are related as

$$\begin{aligned} Re_B &= Re_P \left| \frac{1}{4}\frac{\bar{U}_{GS}}{\bar{D}_B^2} - 1 \right| \bar{D}_B \qquad \text{for expansion stage} \\ &= Re_P \left| \frac{d\bar{Y}}{d\bar{t}} - 1 \right| \left[\bar{D}_{Be}^3 + \frac{3}{2}\bar{U}_{GS}\bar{t} \right]^{1/3} \text{for detachment stage.} \end{aligned} \tag{18}$$

From Eqs. 15 and 16, a functional form of the nondimensional bubble diameter at the point of detachment can be written as

$$\bar{D}_B = f\left(Re_P, We_P, Fr_P, \bar{U}_{GS}, \bar{D}_N, \bar{\rho}\right). \tag{19}$$

For given values of $\bar{U}_{GS}$, $\bar{D}_N$, $\bar{\rho}$, Re_P, We_P, and Fr_P, nondimensional bubble diameter $\bar{D}_B$ is first computed by solving Eq. 15 using the bisection method. The computed $\bar{D}_B$ is the dimensionless bubble diameter at the end of the expansion stage, that is, $\bar{D}_{Be}$. With this information, Eq. 16 is solved using a fourth-order Runge-Kutta method to determine the position of bubble center $\bar{Y}$ and bubble diameter $\bar{D}_B$. For computed values of $\bar{Y}$ and $\bar{D}_B$, the detachment criterion, Eq. 17, is checked. If the limiting condition of Eq. 17 is not satisfied, a small step in time $\Delta\bar{t}$ is taken, all the important forces are recalculated, and Eq. 16 is solved again to obtain a new $\bar{Y}$ and $\bar{D}_B$. At the beginning of the detachment phase $\bar{Y} = 1/2\ \bar{D}_B$. With the increase in time $(\bar{t} + \Delta\bar{t})$, $\bar{Y}$ increases at a faster rate than $1/2\ \bar{D}_B$, and eventually the limiting condition of Eq. 17 is reached when detachment takes place. The computed diameter $\bar{D}_B$ at this point is the detached bubble diameter.

The order of magnitude of various terms in Eq. 16 is observed while solving the equation numerically. It is noted that the principal detaching force is in normal gravity buoyancy, while in reduced and microgravity environment, the most important detaching force is the liquid drag. Out of the two attaching forces, such as bubble inertia and surface tension, the later plays the more important role in preventing detachment.

Experimental Work

Experiments are conducted aboard the Reduced Gravity Research Aircraft at NASA Lewis Research Center. This modified DC-9 aircraft is capable of executing a $2g$ pull-up maneuver followed by a dive trajectory that presents the investigator with a $0.01g$ reduced-gravity environment. Duration of the $0.01g$ trajectory is approximately 20 s, out of which 15-s time is allotted for the acquisition of good-quality, reproducible data. The reproducibility of data between two consecutive trajectories is within $\pm 5\%$. The present coflow configuration experiment is performed with an air–water system. Three different sets of pipe diameter are used: 1.27 cm, 1.9 cm, and 2.54 cm. Two different ratios of nozzle-to-pipe diameter ($\bar{D}_N$), 0.1 and 0.2, are considered. Depending on the two-phase flow-conduit diameter, superficial gas and liquid velocities are varied from 8 to 70 cm/s. The present experimental work considers the following nondimensional parametric ranges: for the 2.54-cm pipe diameter, Re_P = 1,900–5,000, We_P = 2–12, and Fr_P = 2–14; for the 1.9-cm pipe diameter Re_p = 1,600–5,000, We_P = 2–16, and Fr_P = 4–32; and for the 1.27-cm pipe diameter Re_P = 2,000–8,500, We_P = 5–75, and Fr_P = 24–340. For every data point acquired, two dive trajectories are executed in order to ensure data repeatability.

The test section, shown in Figure 2, consists of a Plexiglas pipe that acts as the two-phase flow conduit. A tee-branch fitting is mounted on the inlet side of the pipe. Dry and filtered air is injected through a stainless-steel tube that acts as a nozzle and protrudes into the pipe. Protrusion of the air-injection nozzle inside the pipe is to ensure that the bubble is injected in a region where the surrounding liquid flow is hydrodynamically fully developed. The liquid and gas mixing region within the pipe is surrounded by a Plexiglas visual rectangular box that is filled with water. Its role is to eliminate optical distortion of the generated bubble by matching the refractive index of the coflowing liquid. Distilled water is introduced through the remaining port of the tee-branch fitting. For every experimental run, a new batch of distilled water is used so as to minimize contamination at the bubble surface as much as possible. The test section is integrated within the Learjet Two-Phase Flow Apparatus, developed by

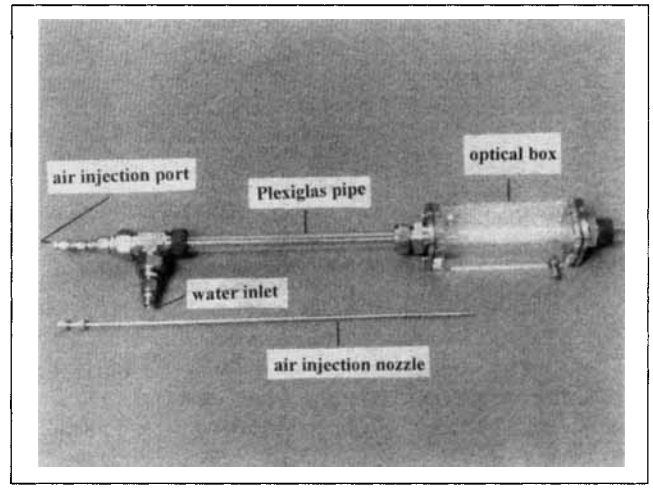

Figure 2. Experimental test section.

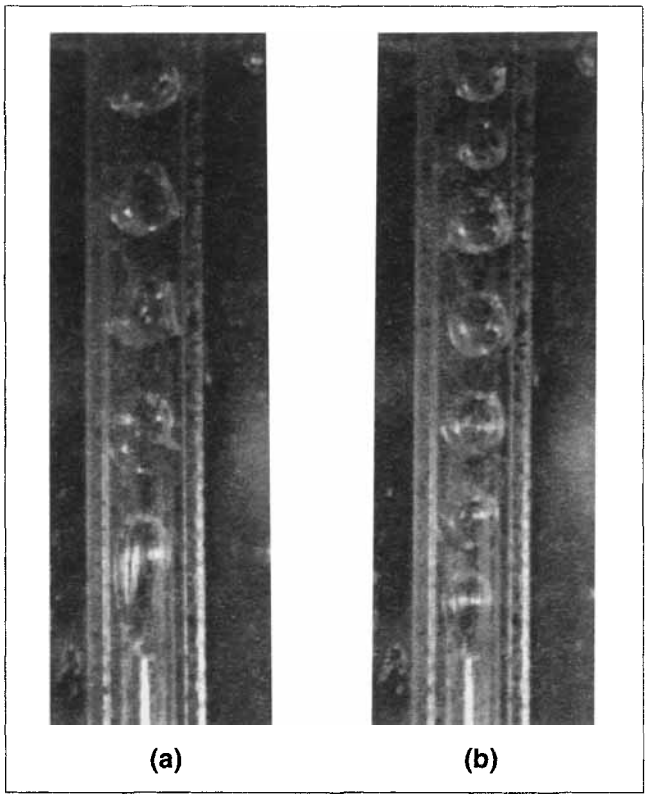

Figure 3. Bubble generation in a 1.27-cm pipe with nozzle-to-pipe diameter ratio 0.2.

(a) High liquid flow; (b) low liquid flow rate.

McQuillen and Neumann (1995). The bubble-generation process is recorded with a high-speed video system (~ 250 frames/second).

A single frame from the experimental video recording at two different flow conditions is shown in Figure 3. Figure 3a shows bubble generation at a relatively high surrounding liquid velocity. It is observed that before detachment the bubble becomes elongated, forming an ellipsoid, due to the inertia effect of the surrounding liquid that dominates over the surface-tension force. Elongation of bubble before detachment, similar to Figure 3a, also occurs at high gas flux when the detached bubble diameter is very close to the pipe diameter ($D_B \rightarrow 1$). On the other hand, at low superficial gas and liquid velocities, as shown in Figure 3b, the shape of the forming bubble is very close to spherical and before detachment it also displays a short-neck region.

Experimental bubble diameter is obtained from the flight experiment video by using THIN 2.0 and OPTIMAS 5.1 image-acquisition and -processing software packages. The geometric averaged bubble diameter for each of the three consecutively detached bubbles in the vicinity of the gas-injection nozzle is first calculated. Bubble diameter reported here is the arithmetic average of these three values. The standard deviation is within $\pm 2.5\%$ of the mean diameter value. Uncertainty errors in flow-velocity measurement have an upper limit of $\pm 5\%$ on the obtained value. Further discussion on experimental procedure and data acquisition is given by Pais (1998).

Results and Discussion

Comparison with experimental results

A comparison of the bubble diameter obtained from the present reduced-gravity experiment with predictions of the numerical model is shown in Figure 4. The figure shows variation of dimensionless bubble diameter, $\bar{D}_B$, with nondimensional superficial gas velocity, $\bar{U}_{GS}$. Two different sets of dimensionless nozzle diameter, $\bar{D}_N$, and for each $\bar{D}_N$, two different Reynolds number Re_P conditions are considered for comparison. For both $\bar{D}_N$ and all Re_P conditions numerical predictions are shown to be within $\pm 10\%$ of the experimental data.

Further comparison of numerically predicted bubble diameter with experimental results is shown in Table 1. A wide range of superficial liquid velocity ($U_{LS} = 8.5$–60.5 cm/s) is considered in this table. These values correspond to $We_P = 1.9$–63.4. It is shown that at high We_P, there is a considerable variation between the numerical and experimental results. At high superficial liquid velocity, that is, at high We_P, the liquid inertia force is considerably higher than the surface-tension force. Since the surface-tension force keeps the bubble spherical, it is evident that at high We_P bubble shape varies substantially from the spherical geometry, causing a change in the drag coefficient and frontal area of the bubble. At such high We_P conditions the theoretical model fails. From the data shown in Table 1, Figure 4, and video frames in Figure 3, it is concluded that under reduced-gravity and microgravity conditions, the present model is valid up to a maximum We_P of 30. Depending on pipe diameter, another parameter coupled with the We_P is the pipe Reynolds number, Re_P. For an air–water system using a 2.54-cm-diameter pipe, $We_P = 30$ corresponds to a Re_P of approximately 7500.

A comparison of numerical and experimental dimensionless bubble-formation time (nondimensionalized as $\bar{t} = tU_{LS}/D_P$) for various $\bar{U}_{GS}$ values is shown in Figure 5. It is seen that for both nozzle diameters ($\bar{D}_N = 0.1$ and 0.2), at

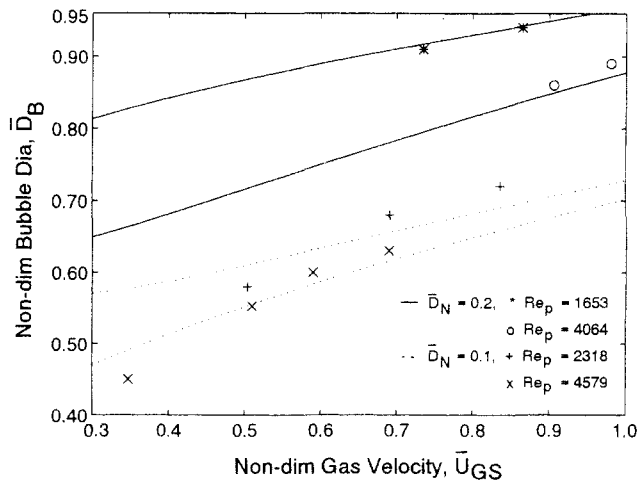

Figure 4. Bubble diameter predictions vs. reduced gravity experimental results at $\bar{\rho} = 0.0012$.

Solid and dotted line: numerical predictions; experimental data: '$*$'— $Re_P = 1{,}653$, $We_P = 1.97$ and $Fr_P = 4.07$; '○'— $Re_P = 4{,}064$, $We_P = 8.93$ and $Fr_P = 10.28$; '+'— $Re_P = 2{,}318$, $We_P = 3.88$ and $Fr_P = 7.99$, and '×'— $Re_P = 4{,}579$, $We_P = 15.13$ and $Fr_P = 31.19$.

Table 1. Experimental vs. Computed Values of Bubble Diameter for Different Flow Conditions in Reduced Gravity, $\bar{D}_N = 0.1$

Flow Conditions	$\bar{U}_{GS}$	Computed $\bar{D}_B$	Exp. $\bar{D}_B$	% Var.
$U_{LS} = 8.5$ cm/s, $Re_P = 1{,}615$	0.753	0.727	0.736	1.22
$We_P = 1.88$, $Fr_P = 3.88$	0.965	0.762	0.815	6.50
$U_{LS} = 10.5$ cm/s, $Re_P = 2{,}667$	0.336	0.572	0.530	7.92
$We_P = 3.84$, $Fr_P = 4.43$	0.567	0.620	0.580	6.90
$U_{LS} = 18$ cm/s, $Re_P = 3{,}420$	0.322	0.503	0.470	7.02
$We_P = 8.44$, $Fr_P = 17.40$	0.822	0.663	0.670	1.04
$U_{LS} = 45$ cm/s, $Re_P = 5{,}740$	0.260	0.432	0.510	15.29
$We_P = 35.57$, $Fr_P = 164.20$	0.540	0.558	0.605	7.77
$U_{LS} = 60.5$ cm/s, $Re_P = 7{,}684$	0.230	0.409	0.570	28.25
$We_P = 63.72$, $Fr_P = 294.20$	0.320	0.459	0.610	24.75

low $\bar{U}_{GS}$, bubble-formation time decreases sharply with increasing $\bar{U}_{GS}$ until it reaches an asymptotic limit, beyond which bubble-formation time remains almost constant, irrespective of the $\bar{U}_{GS}$ value. It is further observed that for all $\bar{U}_{GS}$ values, bubble-formation time is greater for a higher nozzle diameter.

Figure 6 presents a comparison of the normal gravity experimental data obtained by Sada et al. (1978) with current computed results. In their experiment, they injected air through two sets of nozzles of diameters 0.086 cm and 0.305 cm placed at the center of a 5-cm-inner-diameter pipe, through which water flows in the same direction as the injected gas. The surrounding liquid velocity ranged from 11.1 cm/s to 154.9 cm/s, while gas flow rate was varied from 0.83 cm^3/s to 36.2 cm^3/s. For high gas flow rates, they observed bubble coalescence. In Figure 6, only the gas-flow conditions corresponding to the single-bubble regime are shown. In this figure, bubble diameter (D_B in cm) is plotted against volumetric gas flow rate (Q_D in cm^3/s) through a 0.086-cm nozzle

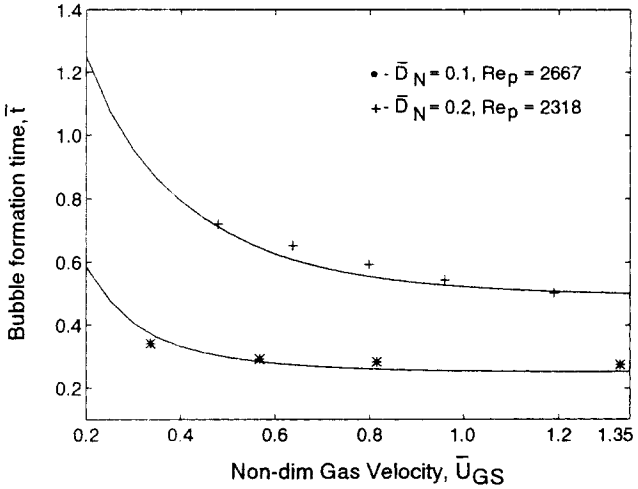

Figure 5. Computed dimensionless bubble-formation time vs. reduced-gravity experimental data.

Solid line: numerical predictions. Experimental data: "$*$"—$\bar{D}_N = 0.1$, $Re_P = 2{,}667$, $We_P = 3.84$, and $Fr_P = 4.43$; and "+"—$\bar{D}_N = 0.2$, $Re_P = 2{,}318$, $We_P = 3.88$, and $Fr_P = 7.99$.

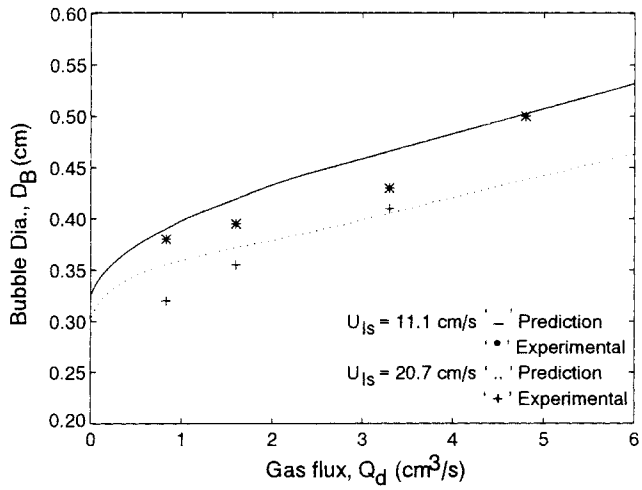

Figure 6. Numerical predictions vs. normal-gravity experimental results (Sada et al., 1978).

Pipe diameter 5 cm and nozzle diameter 0.086 cm. Solid line: computed bubble diameter and "$*$"—experimental bubble diameter at $U_{LS} = 11.1$ cm/s, $Re_P = 5{,}550$, $We_P = 8.44$, $Fr_P = 0.025$; dotted line: computed bubble diameter and "+"—experimental bubble diameter at $U_{LS} = 20.7$ cm/s, $Re_P = 10{,}350$, $We_P = 29.4$, $Fr_P = 0.087$.

for two different coflow liquid velocities ($U_{LS} = 11.1$ cm/s and 20.7 cm/s). The continuous lines show the current computational predictions at Sada's experimental conditions, and the symbols represent their experimental values. While the predictions for these two U_{LS} values are in good agreement ($\pm 10\%$) with the experimental data, further computations for $U_{LS} = 27.6$ cm/s show variations of more than 15%. Once again, this can be attributed to deviation of bubble shape from the spherical geometry assumption at high liquid velocities. For their test-section geometry, the surrounding liquid velocity of 20.7 cm/s corresponds to $We_P = 29.4$. Based on the comparison shown in Figure 6, it is concluded that in normal gravity the upper limit of the Weber number up to which bubble diameter can be predicted from the present model is $We_P = 30$.

Range of dimensionless variables

At high gas flow rate, a detached bubble and a forming bubble at the nozzle tip can merge, causing bubble coalescence at the nozzle exit. It is experimentally observed (Pais, 1998) that immediately after detachment, the rear end of the bubble flattens out, thereby moving further away from the nozzle tip. Subsequently, the rear end of the detached bubble expands and the bubbles resumes its spherical shape. During this expansion process, the rear end of the bubble moves toward the nozzle tip. At high gas injection flux, while the rear end of the detached bubble undergoes flattening and subsequent expansion, another bubble is formed at the nozzle tip. It is possible for the front of this forming bubble to catch up with the rear end of the detached bubble, especially when the latter is expanding. This merger of the two distinct bubble fronts results in coalescence and forms a larger bubble. A coalesced bubble can be smaller than the pipe diameter or can result in slug formation. For a fixed superficial liquid velocity, the onset of the coalescence condition is characterized

by a critical gas flux. In dimensionless form, the onset condition can be described by a critical nondimensional superficial gas velocity $\bar{U}_{GS_{crit}}$. It is experimentally observed (Pais, 1998, and Sada et al., 1978) that $\bar{U}_{GS_{crit}}$ depends on nozzle diameter. In the present reduced-gravity experiment, the critical $\bar{U}_{GS}$ for the onset of coalescence for $\bar{D}_N = 0.1$ is observed to be 1.35. The present article focuses on single-bubble generation. Therefore, for the predictions of results under microgravity conditions, discussed in the following subsection, the upper limit of $\bar{U}_{GS}$ is chosen to be 1.35.

In reduced- and microgravity environments, a single spherical bubble can grow up to the size of the pipe diameter before it detaches ($D_B = D_P$ or $\bar{D}_B = 1$). If the bubble does not detach at this point, it changes shape to form a long Taylor bubble. Theoretically, the current model can predict nondimensional bubble diameter up to $\bar{D}_B = 1$. However, it is noted that before detachment, if the bubble grows close to $\bar{D}_B = 1$, it blocks the surrounding liquid flow, thereby constricting the liquid-flow area. This situation leads to high local liquid velocity, and therefore high liquid inertia. In the competition between liquid inertia and surface tension, the former prevails, thus causing the bubble to deviate from its spherical shape. As a result, the bubble assumes an elongated shape, similar to the picture shown in Figure 3a. The drag coefficient and the frontal area of an elongated bubble are different from those of a spherical bubble, as used in this model. The present theoretical work does not take into account the variation in drag force due to change of shape and therefore cannot be used for accurate prediction of $\bar{D}_B$ in the vicinity of 1. Figure 4 shows that under reduced gravity conditions, the prediction of the present model agrees well with the experimental $\bar{D}_B$ of 0.94. Keeping this in mind, the cutoff $\bar{D}_B$ is taken to be 0.95 in all of the following predictions.

Predictions of bubble formation in microgravity

The present model is applied to predict bubble diameter under reduced- and microgravity environments. The effects of flow conditions, injection geometry, and fluid properties on the bubble-formation process are investigated. Dependence of bubble diameter, D_B, on the superficial gas velocity, U_{GS} (or volumetric gas flow rate $Q_d = (\pi/4)D_P^2 U_{GS}$, for a fixed pipe diameter), and nozzle diameter, D_N, is shown in Figure 7. By fixing nondimensional parameters $\bar{\rho} = 0.0012$, $We_P = 0.912$, $Re_P = 1{,}300$, and $Fr_P = 105.25$, dimensionless bubble diameter, $\bar{D}_B$, is obtained as a function of nondimensional superficial gas velocity, $\bar{U}_{GS}$, and dimensionless nozzle diameter, $\bar{D}_N$. The dimensionless parameters used in this plot correspond to air injection in coflowing water. Figure 7 shows that $\bar{D}_B$ increases steadily with $\bar{U}_{GS}$, indicating a direct proportionality between the bubble diameter and the gas flux. All the detaching forces acting on the bubble, such as momentum flux, liquid drag, and reduced buoyancy under microgravity conditions, increase with increasing gas injection rate. At the same time, bubble inertia force, which acts as an attaching force, also increases, at a much faster rate. Consequently, the inertia force outweighs the effects of the detaching forces, thereby increasing $\bar{D}_B$ with $\bar{U}_{GS}$. Furthermore, Figure 7 shows an increasing trend of bubble diameter with nozzle diameter, which can be explained by the detaching effect of momentum flux. For the same gas flow rate (constant

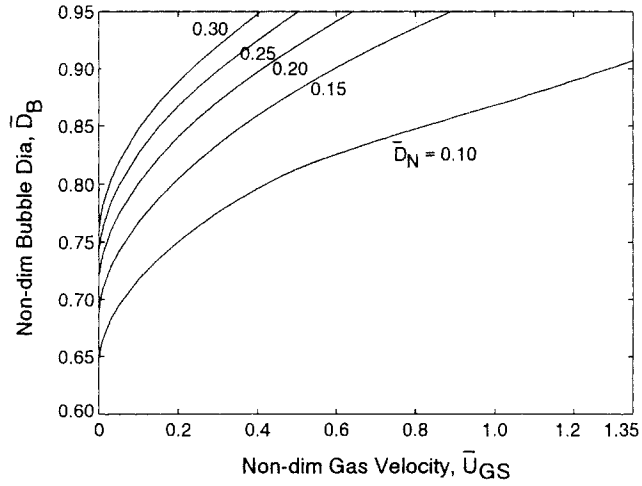

Figure 7. Variation of dimensionless bubble diameter $\bar{D}_B$ with dimensionless superficial gas velocity $\bar{U}_{GS}$ for various nozzle diameters $\bar{D}_N$.

$\bar{\rho} = 0.0012$, $Fr_P = 105.25$, $We_P = 0.912$, and $Re_P = 1{,}300$.

$\bar{U}_{GS}$), an increase in nozzle diameter causes a reduction in gas-momentum flux, thus increasing the bubble diameter. It is evident that the effect of $\bar{D}_N$ is more prominent at high $\bar{U}_{GS}$. At low $\bar{U}_{GS}$ the momentum flux is low and the overall force balance is dominated by other forces, whereas, at high $\bar{U}_{GS}$, when the momentum flux is high, a change in nozzle diameter has a more significant impact on the overall force balance, and thus on bubble diameter. It is further observed that at $\bar{D}_N = 0.1$, a Taylor Bubble is not formed from a single bubble in the considered range of $\bar{U}_{GS}$. As predicted earlier, however, coalescence takes place for $\bar{U}_{GS} \geq 1.35$ and the coalesced bubble can cause a slug to develop. For higher values of $\bar{D}_N$, the critical $\bar{U}_{GS}$ for coalescence is higher than 1.35. The plot shows that for $\bar{D}_N = 0.2$ or higher, even before coalescence, a single bubble undergoes transition from bubbly to slug flow at a much lower superficial gas velocity. With an increase in $\bar{D}_N$ from 0.2 to 0.3, transition from bubbly to slug flow takes place at a lower $\bar{U}_{GS}$.

The effect of superficial liquid velocity U_{LS}, and gravity level, g, on bubble diameter, D_B, is shown in Figure 8. For a set of continuous- and dispersed-phase fluids (constant ρ_c, ρ_d, μ_c, μ_d, and σ) with constant gas-flow condition (U_{GS} constant) and fixed geometry (constant D_P and D_N), bubble diameter is computed for various U_{LS} and g-level conditions. The 1g and 3g computations shown in this figure are carried out for the configuration shown in Figure 1, that is, when buoyancy assists bubble detachment. As U_{LS} is increased, all the nondimensional numbers, such as Reynolds number Re_P, Weber number We_P, Froude number Fr_P, and dimensionless superficial gas velocity $\bar{U}_{GS}$, change. However, the product of $\bar{U}_{GS}$ and Re_P ($Re_P \bar{U}_{Gs} = \rho_c U_{GS} D_P/\mu_c$) and the ratio of We_P to Fr_P, defined as the Bond number [$Bo = We_P/Fr_P = (\rho_c - \rho_d) g D_P^2/\sigma$] remain constant. Figure 8 shows variation of $\bar{D}_B$ with Re_P for various Bo values, representing different g levels. It is evident that $\bar{D}_B$ shows a decreasing trend with the increase of Re_P. This is due to the fact that with the increase of U_{LS} and thus Re_P, the detaching effect of liquid drag and inertia increases, thereby reducing bubble diameter. It is fur-

ther seen that under microgravity conditions ($Bo = 0.0087$), there is a great deal of variation in $\bar{D}_B$ in the range of $Re_P = 500$ to $Re_P = 5{,}000$. On the other hand, in normal gravity ($Bo = 87$), bubble diameter decreases only by a small amount over the entire range of Re_P. At the 3g condition ($Bo = 260$), the variation is even less and the bubble diameter remains almost constant. In normal gravity, the buoyancy force overwhelms the effect of liquid drag and inertia. Thus the increase of U_{LS} does not show a significant reduction effect on bubble diameter. At the 3g condition, under stronger buoyancy force than normal gravity, the liquid drag effect on bubble diameter is further lowered. On the other hand, under microgravity conditions, liquid drag plays the key role in bubble detachment. Therefore, a change in U_{LS} affects the bubble diameter considerably. The detaching effect of the buoyancy force also explains the difference in bubble size at different gravity environments, as shown in Figure 8. It is observed that at a fixed Re_P, as gravity is reduced, by reducing Bo, larger bubbles are formed. It is to be noted, however, that there is a saturation effect of the reduction of gravity. The microgravity curve shown in Figure 8 represents bubble diameter at $10^{-4}g$ condition. Bubble diameter at reduced-gravity condition ($0.01g$) is slightly less than that of the microgravity condition, the difference being barely detectable. This indicates that at $0.01g$ environment, the buoyancy effect is already significantly reduced. Any further reduction of the gravity environment does not make a significant difference in the force-balance equation and therefore on the bubble diameter.

Figure 9 displays the modified nondimensional bubble diameter D_B^* as a function of nondimensional superficial gas velocity $\bar{U}_{GS}$ for various pipe diameter D_P conditions. Here the bubble diameter is nondimensionalized with respect to nozzle diameter ($D_B^* = D_B/D_N$). In order to study the effect of pipe diameter D_P on bubble diameter D_B, the volumetric flux of liquid (Q_c) and gas (Q_d) are kept constant. For the same Q_c an increment in D_P causes a reduction of the dimensionless parameters, such as Reynolds number Re_P, Weber number We_P, Froude number Fr_P, and dimensionless nozzle diameter $\bar{D}_N$. It is observed that at a fixed $\bar{U}_{GS}$, as D_P is increased, bubble diameter increases. Under constant Q_c and Q_d conditions, an increase in D_P implies reduction of superficial liquid velocity U_{LS}, and thereby a reduction of the detaching effect of liquid drag and inertia. This explains the increasing trend of bubble diameter with pipe diameter. Over the entire range of $\bar{U}_{GS}$, the effect of pipe diameter remains similar. The maximum value of $\bar{U}_{GS}$ used in this figure is 0.95. It is evident from this figure that at $\bar{U}_{GS} = 0.95$, D_B^* approaches a value of 5, which corresponds to $\bar{D}_B = D_B^* \bar{D}_N = 1$. As indicated in the previous section, the maximum value of $\bar{D}_B$ that can be predicted using this model is 0.95. Therefore, to ensure that predictions do not go beyond $\bar{D}_B = 0.95$, the present calculation is stopped at $\bar{U}_{GS} = 0.95$.

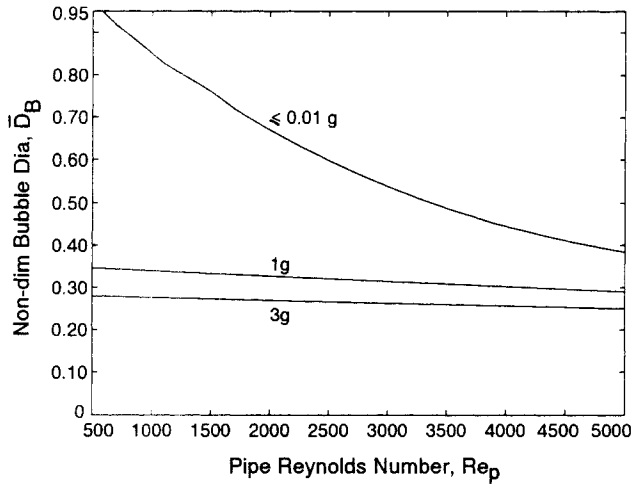

Figure 8. Variation of nondimensional bubble diameter $\bar{D}_B$ with Reynolds number Re_P for different Bond numbers Bo.

$\bar{p} = 0.0012$, $\bar{D}_N = 0.1$, and $Re_P \bar{U}_{GS} = 500$. $\leq 0.01g$ curve— $Bo \leq 0.867$; $1g$ curve— $Bo = 86.7$; and $3g$ curve— $Bo = 260.1$.

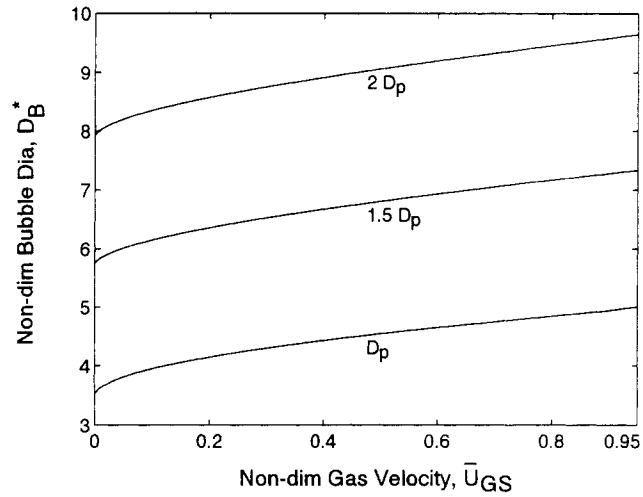

Figure 9. Variation of nondimensional bubble diameter D_B^* with nondimensional superficial gas velocity $\bar{U}_{GS}$ for different pipe-diameter conditions.

Fixed $\bar{p} = 0.0012$. D_P curve— $\bar{D}_N = 0.20$, $Re_P = 1{,}000$, $We_P = 1.1$, $Fr_P = 498$; $1.5D_P$ curve— $\bar{D}_N = 0.133$, $Re_P = 667$, $We_P = 0.32$, $Fr_P = 65.5$; $2D_P$ curve— $\bar{D}_N = 0.1$, $Re_P = 500$, $We_P = 0.136$, $Fr_P = 15.5$.

Variation of dimensionless bubble diameter, $\bar{D}_B$, with nondimensional superficial gas velocity $\bar{U}_{GS}$ and We_P is shown in Figure 10. It is seen that for all We_P, $\bar{D}_B$ increases steadily with $\bar{U}_{GS}$. In other words, bubble diameter increases with gas-momentum flux. Figure 10 further shows the effect of surface tension on bubble diameter under microgravity conditions. At a fixed $\bar{U}_{GS}$, as surface tension is increased by reducing We_P, the bubble diameter increases. This is attributed to the attaching effect of surface tension.

Dependence of bubble diameter on surrounding liquid viscosity is shown in Figure 11. In this figure curves 2, 3, and 4, respectively, correspond to liquid dynamic viscosity twice, five times, and ten times that of curve 1. All other dimensionless parameters are held constant, while the Reynolds number is reduced from curve 1 to curve 4. A more viscous liquid induces a higher liquid drag. At the range of considered Re_P, coflowing liquid velocity (U_{LS}) is always higher than the bubble center velocity (ds/dt). Therefore liquid drag acts as a detaching force. This explains the formation of smaller bubbles in a more viscous liquid environment. It is further seen

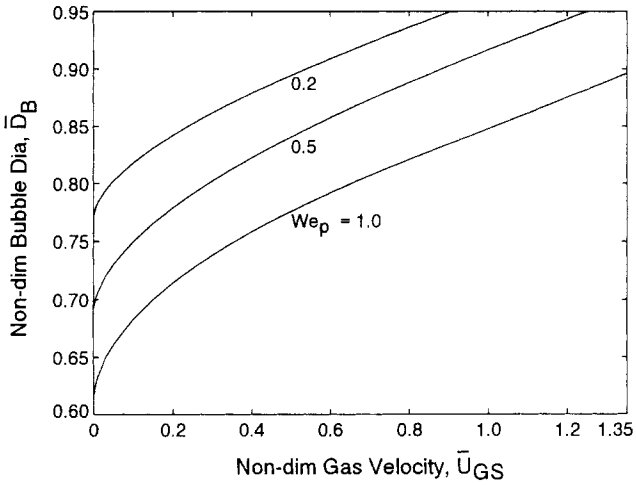

Figure 10. Variation of dimensionless bubble diameter $\bar{D}_B$ with dimensionless superficial gas velocity $\bar{U}_{GS}$ for various Weber numbers We_P.

$\bar{\rho} = 0.0012$, $Fr_P = 22.42$, $Re_P = 600$, and $\bar{D}_N = 0.1$.

that the effect of liquid viscosity decreases at high $\bar{U}_{GS}$ and the curves tend to converge. This indicates a diminishing role of liquid drag in the overall force balance at high gas flux conditions.

Conclusion

The present work concentrates on single-bubble generation in the dynamic and bubbly flow regime, and investigates the onset of bubble coalescence. The article reports a study of bubble formation for constant gas flux injected through a single nozzle in a coflowing liquid configuration. The described theoretical model predicts bubble diameter at detachment, in good agreement with both reduced- and normal-gravity experiments. A force-balance equation, describing the overall bubble dynamics, is developed for the two stages of bubble generation, namely the expansion stage and the detachment stage. Two sets of forces, one aiding and the other inhibiting bubble detachment, and thereby controlling bubble size, are identified. The gas flux and buoyancy, under normal gravity conditions, aid, while the bubble inertia and surface-tension force at the nozzle rim, detract, from bubble detachment. On the other hand, liquid drag and inertia have a dual role. In other words, they can act both as detaching or attaching forces, a fact that depends on the relative velocity of the bubble with respect to the surrounding liquid.

The effects of the coflowing liquid properties, flow conditions, and injection geometry on bubble size are investigated. It is observed that with a reduction in the gravity field, larger bubbles are formed. Bubbles in the reduced-gravity environment are shown to be larger and more spherical than those in the terrestrial environment. It is further observed that reduction of the gravity field below the reduced-gravity environment ($0.01g$) does not have a significant impact on bubble size. Therefore, bubbles in the microgravity environment are only slightly larger than those in the reduced-gravity environment, the difference being barely noticeable. Both under normal- and microgravity conditions, bubble diameter decreases with increasing superficial liquid velocity, the effect being more predominant in microgravity. It is further noted that bubble size increases with increasing pipe and nozzle diameters. Furthermore, increasing liquid density and viscosity enhance the bubble detachment process, while surface tension plays an inhibiting role.

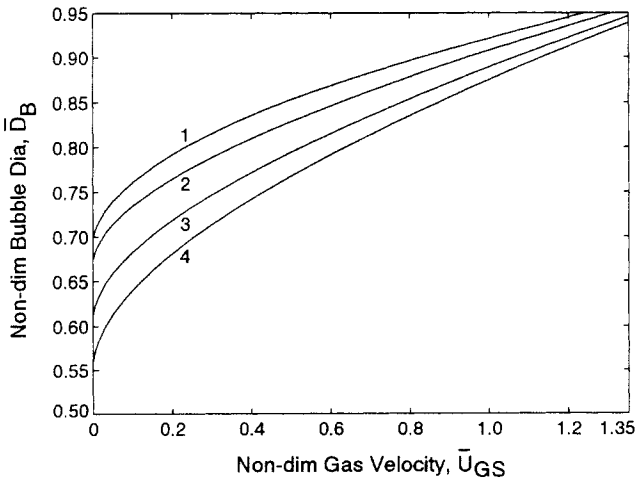

Figure 11. Variation of dimensionless bubble diameter $\bar{D}_B$ with dimensionless superficial gas velocity $\bar{U}_{GS}$ for various coflowing liquid viscosities.

$\bar{\rho} = 0.0012$, $Fr_P = 62.21$, $We_P = 0.54$, and $\bar{D}_N = 0.1$. Curve (1)— $Re_P = 1{,}000$; curve (2)— $Re_P = 500$; curve (3)— $Re_P = 200$; and curve (4)— $Re_P = 100$.

Acknowledgment

We gratefully acknowledge support from the National Aeronautics and Space Administration, Grant No. NAG3-1913, which made this work possible.

Literature Cited

Al-Hayes, R. A. M., and R. H. S. Winterton, "Bubble Growth in Flowing Liquids," *Int. J. Heat Mass Transfer*, **24**, 213 (1981).

Banerjee, S., "Space Applications," Multiphase Flow and Heat Transfer: Bases and Applications Workshop, Santa Barbara, CA (1989).

Bird, R. B., W. E. Stewart, and E. N. Lightfoot, *Transport Phenomena*, Wiley, New York (1960).

Buyevich, Y. A., and B. W. Webbon, "Bubble Formation at a Submerged Orifice in Reduced Gravity," *Chem. Eng. Sci.*, **51**, 21 (1996).

Chuang, S. C., and V. W. Goldschmidt, "Bubble Formation Due to a Submerged Capillary Tube in Quiescent and Co-Flowing Systems," *J. Basic. Eng.*, **92** (1970).

Clift, R., J. R. Grace, and M. E. Weber, *Bubbles, Drops, and Particles*, Academic Press, New York (1978).

Colin, C., J. Fabre, and A. E. Dukler, "Gas-Liquid Flow at Microgravity Conditions: I. Dispersed Bubble and Slug Flow," *Int. J. Multiphase Flow*, **17**, 4 (1991).

Colin, C., J. Fabre, and J. B. McQuillen, "Bubble and Slug Flow at Microgravity Conditions: State of Knowledge and Open Questions," *Chem. Eng. Commun.*, **141/142**, 4 (1996).

Dukler, A. E., J. A. Fabre, J. B. McQuillen, and R. Vernon, "Gas-Liquid Flow at Microgravity Conditions: Flow Patterns and Their Transitions," *Int. J. Multiphase Flow*, **14**, 4 (1988).

Hahne, E., and U. Grigull, *Heat Transfer in Boiling*, Hemisphere, New York (1977).

Herold, K. E., and K. R. Kolos, "Bubbles Aboard the Shuttle," *Mech. Eng.*, **119**, 10 (1997).

Hill, T. J., "Gas-Liquid Flow Challenges in Oil and Gas Production," ASME Fluids Engineering Division Summer Meeting, Vancouver, BC (1997).
Jayawardena, S. S., V. Balakotaiah, and L. C. Witte, "Flow Pattern Transition Maps for Microgravity Two-Phase Flows," *AIChE J.*, **43**, 6 (1997).
Kawase, Y., and J. J. Ulbrecht, "Formation of Drops and Bubbles in Flowing Liquids," *Ind. Eng. Chem. Process Des. Dev.*, **20**, 636 (1981).
Kim, I., "Modeling of Bubble and Drop Formation in Flowing Liquids in Terrestrial and Microgravity Environments," PhD Thesis, Case Western Reserve Univ., Cleveland, OH (1992).
Kim, I., Y. Kamotani, and S. Ostrach, "Modeling Bubble and Drop Formation in Flowing Liquids in Microgravity," *AIChE J.*, **40**, 1 (1994).
Klausner, J. F., R. Mei, D. M. Bernhard, and L. Z. Zeng, "Vapor Bubble Departure in Forced Convection Boiling," *Int. J. Heat Mass Transfer*, **36** (1993).
Kumar, R., and N. R. Kuloor, "The Formation of Bubbles and Drops," *Adv. Chem. Eng.*, **8** (1970).
McCann, D. J., and R. G. H. Prince, "Regimes of Bubbling at a Submerged Orifice," *Chem. Eng. Sci.*, **26** (1971).
McQuillen, J. B., and E. S. Neumann, "Learjet Two Phase Flow Apparatus," NASA Tech. Memo. 106814, NASA Lewis Research Center, Cleveland, OH (1995).
Ostrach, S., "Industrial Processes Influenced by Gravity," NASA Reps. CR-182140, C-21066-G, NASA, Washington, DC (1988).
Pais, S. C., "Bubble Generation Under Reduced Gravity Conditions," PhD Thesis, Case Western Reserve Univ., Cleveland, OH (1998).
Pamperin, O., and H. Rath, "Influence of Buoyancy on Bubble Formation at Submerged Orifices," *Chem. Eng. Sci.*, **50**, 19 (1995).
Räbiger, N., and A. Vogelpohl, "Bubble Formation and Its Movement in Newtonian and Non-Newtonian Liquids," *Encyclopedia of Fluid Mechanics*, Vol. 3, Gulf Pub., Houston (1986).
Ramakrishnan, S., R. Kumar, and N. R. Kuloor, "Studies in Bubble Formation: I. Bubble Formation Under Constant Flow Conditions," *Chem. Eng. Sci.*, **24** (1969).
Sada, E., A. Yasunishi, S. Katoh, and M. Nishioka, "Bubble Formation in Flowing Liquid," *Can. J. Chem. Eng.*, **56** (1978).
Tsuge, H., "Hydrodynamics of Bubble Formation from Submerged Orifices," *Encyclopedia of Fluid Mechanics*, Vol. 3, Gulf Pub., Houston (1986).
Van Krevelen, D. W., and P. J. Hoftijzer, "Studies of Gas-Bubble Formation–Calculation of Interfacial Area in Bubble Contractors," *Chem. Eng. Prog.*, **46**, 29 (1950).
Wraith, A. E., "Two Stage Bubble Growth at a Submerged Plate Orifice," *Chem. Eng. Sci.*, **26** (1971).
Zeng, L. Z., J. F. Klausner, and R. Mei, "A Unified Model for the Prediction of Bubble Detachment Diameters in Boiling Systems: I. Pool Boiling," *Int. J. Heat Mass Transfer*, **36**, 9 (1993).

Manuscript received Jan. 13, 1998, and revision received Apr. 30, 1998.